20th Australasian Fluid Mechanics Conference
Perth, Australia
5-8 December 2016

Flow and heat-transfer under circular jet-impingement on a vibrating impingement surface

T Natarajan[1], J Jewkes[2], A D Lucey[1], R Narayanaswamy[1] and Y M Chung[3]

[1]Fluid Dynamics Research Group
Dept. of Mechanical Engineering, Curtin University, Perth, Australia 6845.

[2]School of Mechanical, Aerospace and Automotive Engineering,
Coventry University, Coventry CV1 5FB, U.K.

[3]School of Engineering and Centre for Scientific Computing
University of Warwick, Coventry CV4 7AL, U.K.

Abstract

Large-eddy simulation of a circular turbulent jet impinging on a flat excited wall supplied with a uniform heat-flux are considered at a jet Reynolds number, Re_D = 10000 at a mean nozzle-to-wall spacing, h/D = 2.0. The frequency of wall excitation, f_w, is chosen such that the frequencies are sub-harmonic and harmonic to the natural frequency or the preferred mode, f_n, of the impinging jet. The amplitude of vibration, A, is fixed at $0.25D$. Baseline simulations are performed for circular jet impingement on a static impingement wall to validate the methodology adopted herein. The natural frequency (f_n) of the jet is found to be 120 Hz and correspondingly, the wall excitation frequencies (f_w) at the preferred mode of 120 Hz and at sub-harmonic mode of 60 Hz is chosen for investigation. Additionally, LES for a jet Reynolds number, Re_D = 23000 and a wall excitation frequency, f_w = 100 Hz show that the thermal imprints on the impingement wall are strongly influenced by the wall excitation frequencies and enhancement in heat-transfer was observed in the stagnation region. Both the primary and the secondary Nusselt number peaks were observed with the latter found to shift correlating with the convecting large eddies. Since the convection of these eddies can be modulated with the impingement wall excitation frequency, control of the primary and secondary peak to achieve optimum heat-transfer under such dynamic configurations is possible.

Introduction

The importance of jet impingement cannot be underestimated with the volume of published literature extending over a few decades (e.g. [6], [1], [2], [13]). Because of its simple configuration, impinging jets find applications in several process and product industries for effective heat removal (cold jets) and heat addition (hot jets). The net effect of the impingement heat-transfer is a strong function of the impingement surface properties such as thermal conductivity, porosity, and physical state such as static or vibrating. Previous literature on impinging jets have, by and large, been dedicated to jets impinging on static surfaces. Moving surfaces, surfaces with protrusions and impingement on rotating components have been investigated to a certain extent over the past decade. The present research investigates the effect of one such geometrical aspect where the impingement surface undergoes vibration. It essentially investigates and seeks to understand the inherent complexities involved in terms of numerical modelling and the physics in the domain whilst analysing such configurations. Large-eddy simulations of a circular turbulent jet impinging on a flat excited wall supplied with a uniform heat-flux are considered at a jet Reynolds number, Re_D = 10000 (based on jet diameter, D) at a mean nozzle-to-wall spacing, h/D = 2.0. Two surface vibration frequencies at 60 Hz and 120 Hz are used to gauge the effect on the configuration. The amplitude of vibration, A, is fixed at 0.25 D. The paper initially presents the computational methodology, grid construction and boundary conditions followed by the validations and discussion of preliminary results of flow field and heat transfer data before arriving at conclusions.

Computational Methodology

The simulations were performed using large-eddy simulations (LES) with the C++ library OpenFOAM [14] to solve the incompressible Navier-Stokes equations discretised on a uniform Cartesian grid. The subgrid scale modeling was performed with the dynamic Smagorinsky model with a modification proposed by Lilly [10]. Time discretisation is performed with a second-order accurate backward implicit scheme and the convection terms are discretised with a central-differencing scheme. The pressure-velocity coupling is solved with PISO–SIMPLE (PIMPLE), an algorithm that merges Pressure Implicit with Splitting of Operator algorithm (PISO) and a Semi-Implicit Method for Pressure-Linked Equations (SIMPLE) algorithm that allows the calculation of pressure on a mesh from velocity components by coupling the Navier–Stokes equations through iterations. The temporal resolution is dynamically adjusted through a variable time-stepping technique such that the Courant-Friedrich-Lewy (CFL) number was less than or equal to 0.5 at all times. The code is parallelized using the Message Passing Interface (MPI) protocol and the graph partitioning algorithm SCOTCH was used to decompose the solution domain into the required number of sub-domains for parallel computing. Since this algorithm reduces the number of processor boundaries, thus reducing the interconnect message passing, it results in higher performance. The simulations were carried out on MAGNUS, a Cray XC40 supercomputing system located at the Pawsey Supercomputing Centre, Western Australia.

Grid and boundary conditions

A schematic of the flow configuration is presented in figure 1. The solution domain is a collocated grid system with Cartesian coordinates, $\mathbf{X} = (x, y, z)$; with the origin at the center of the domain Ω, where $\Omega = [0, r] \times [0, L_y]$ with $L_y = 9D$ and the radius, $r = 10D$. The instantaneous velocity components are denoted $\mathbf{u} = (u, v, w)$ and the mean velocity components are denoted by $\mathbf{U} = (U, V, W)$. In the (x, y)-plane, the radial direction $r = \sqrt{x^2 + z^2}$ is given by x (at azimuthal direction, z = 0) and the azimuthal angle $\theta = \arctan(x/z)$.

Care was taken to cluster the cells from the inlet to the stagnation zone ($0 < r < 0.3D, 0 < L_y < 9D$). The circular shape of the domain was discretised with a 'butterfly' mesh topology that is based on a square outline at the centre and gradually modified into the circular shape. The geometric expansion ratio of the mesh was maintained below 1.2 for the mesh to expand smoothly in the radial direction in the critical areas

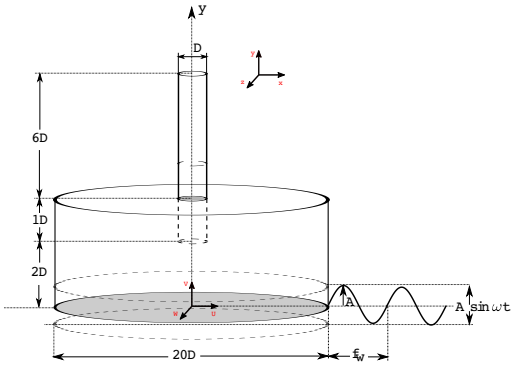

Figure 1: Schematic of the configuration

of interest. In the region close to the pipe/nozzle wall region ($0.3 < r < 0.5D, 0 < L_y < 9D$), the mesh was finely graded from the nozzle wall towards the axis centreline. It is critical to have a fine mesh in this area to resolve the near-wall statistics of the inflow such as axial-and wall-normal components of fluctuations which directly influence the impingement-wall heat-transfer. The region immediately at the nozzle exit ($1.75D < L_y < 2.2D$), is arrayed with cells and graded with a finer mesh so that the instabilities generated due to the shear and sudden expansion of the fluid upon exit are captured effectively. Finally, in the near-wall region the cells are configured in uniform annular layers and graded such that maximum $y^+_{wall} \approx 1.0$ which is within the viscous sub-layer. The majority of the cells were arrayed within the region $0 < L_y < 1D$ and $-4D < r < 4D$ so as to resolve the shear layer development. All the grids are discretised with hexahedral control volumes.

At the inlet, fully-developed turbulent flow is generated by the recycle plane at an upstream distance of $1D$ from the nozzle-exit. At the impingement wall, $y = 0$, a predefined mesh motion prescribed by a moving wall boundary condition is implemented via a Dirichlet (no-slip) boundary condition. For pressure, a Neumann boundary condition is used which implies $\partial p/\partial y = (x, y = 0, z) = 0$ and a uniform heat-flux boundary condition is applied at the wall for temperature. On the bounding sides of the domain (i.e., $r/D = \pm 10$, and $y/D = L_y/3$), a mixed boundary condition is applied for velocity where $\mathbf{U}$ is evaluated from the flux when the pressure is known. Turbulence statistics are averaged in space and time after 10 flow cycles where one flow cycle means that a fluid particle has travelled through the axial and radial dimensions i.e. $9D + 10D$ at the bulk velocity, V_b. The statistical averaging is continued for 30 flow cycles. The entire domain was initialized with a converged Reynolds-averaged Navier–Stokes (RANS) simulation.

Results

Code validation

The initial code validation is performed for a pipe flow to validate the method of generating fully developed turbulent inflow and then applied to a static wall case with the jet Reynolds number, Re_D = 23000. The results are then presented for Re_D = 10000 with both static and moving walls. Generation of turbulent inflow is performed by mapping the data at the inlet from a plane located at a specific downstream distance, (L_{map}). Several studies (see [5], [7], [11]) have reported that a domain length of $8D$ is sufficient to capture the large-scale motions and thus the recycle plane location, L_{map} = $5D$ is chosen. Figure 2 shows the rms velocities and the Reynolds shear stress obtained for pipe flow using the recycled boundary condition for a Reynolds number, Re_p = 24600 based on the pipe diameter. Excellent agreement is observed with the present

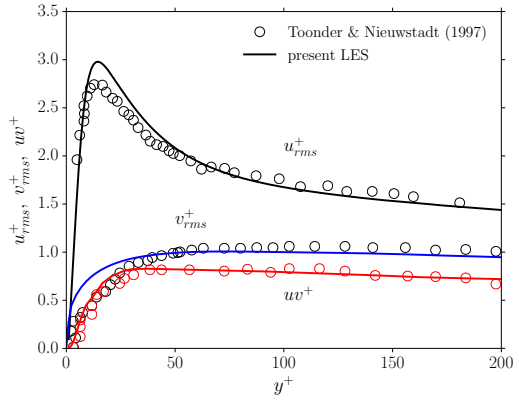

Figure 2: RMS and shear stress results of the pipe flow simulations compared with the experiments of Toonder and Nieuwstadt [4]

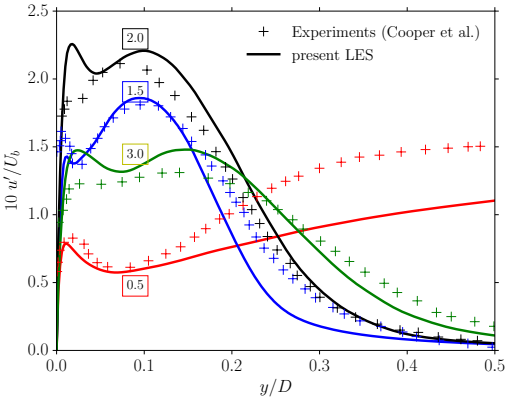

Figure 3: Time averaged radial rms fluctuations for Re_D = 23000 and h/D = 2.0 at r/D = 0.5, 1.5, 2.0 & 3.0.

method of generating fully-developed turbulent inflow. Using the above–mentioned method of generating a fully-developed turbulent inflow, we validate our system model against a conventional jet-impingement case of Cooper et al. [2] and Baughn & Schimizu [1] at a jet Reynolds number, Re_D = 23000 and a stand-off distance h/D = 2.0. Figure 3 shows the axial fluctuations at different radial directions. Good agreement is observed with the experiments. For detailed discussion and analysis the reader is referred to Natarajan et al. [12].

Static Wall case at Re_D = 10000

Figure 4 shows the power spectra of velocity signals measured at several locations using diagnostic points (P1 to P5) in the

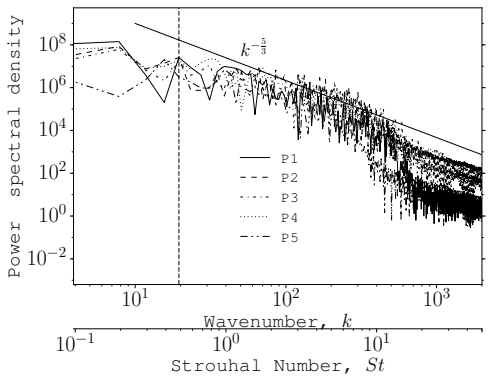

Figure 4: Power spectra in the domain for static wall case at Re_D = 10000.

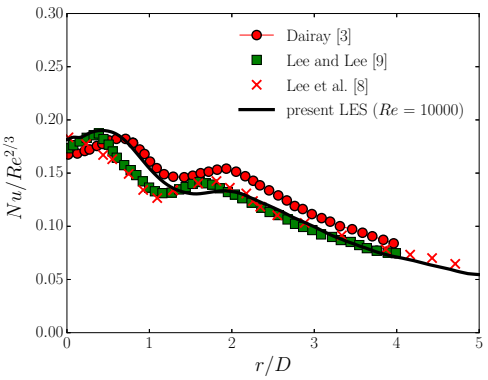

Figure 5: Time averaged radial Nusselt number for Re_D = 10000 for the static wall case compared with experiments of Lee and Lee [9], Lee et al. [8] and DNS of Dairay et al [3].

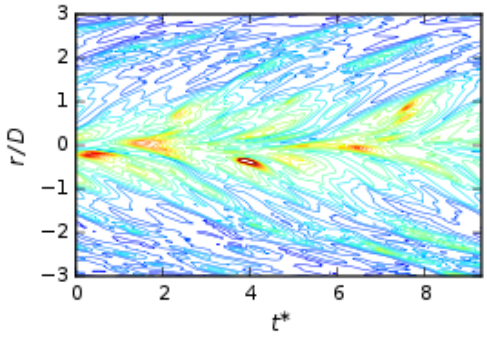

Figure 6: Space-time contours of instantaneous Nusselt number for the static wall case at Re_D = 10000

shear layer of the jet for a static wall case at Re_D = 10000 and its corresponding heat transfer in the form of time averaged radial Nusselt number ($Nu = q'D/\lambda$, where, q' is the heat transfer coefficient, D, the jet diameter and λ, the thermal conductivity of the fluid) is shown in figure 5. The power spectra shows a weak peak frequency corresponding to a Strouhal number, St = 0.45 (defined as $St = f_nD/U$ & marked in the figure 4 with a dotted line) which corresponds to the natural jet frequency, f_n = 120 Hz. As the flow is fully-developed, a single clear dominant frequency is not clearly visible in the spectra. However, this value of Strouhal number (St) is within the range reported for similar cases.

The resulting heat transfer data (figure 5) agrees well with previous experimental data (see [9], [8]) and DNS data [3]. The conventional space-time contour of Nusselt number for Re_D = 10000 is shown in figure 6. Due to the highly unsteady and turbulent nature of the impinging flow, the impingement heat transfer shows complex streaky patterns. The footprints of the large eddy structures visualized, correspond to St = 0.45.

Vibrating Wall case at Re_D = 10000

We now consider the jet-impingement case with a vibrating wall for a jet Reynolds number, Re_D = 10000. The frequency of wall excitation, f_w, is chosen such that the frequencies are sub-harmonic to the natural frequency or the preferred mode, f_n, of the impinging jet. Correspondingly, the frequency of vibration f_w is set to 60 Hz and 120 Hz. The amplitude of vibration, A, is fixed at 0.25 D.

The flow field in the domain is shown in figure 7 when the impingement surface reaches its positive maximum (i.e 1.75D from the jet-exit). The flow field exhibits all the typical regions expected in a canonical jet-impingement flow which are the jet

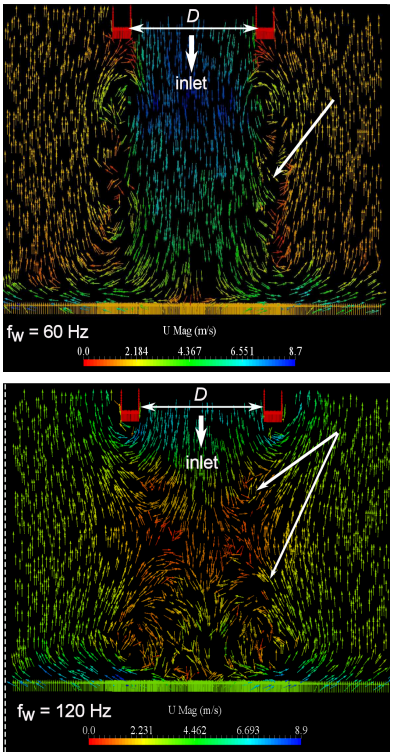

Figure 7: Flow field visualization with velocity vectors showing the effect of vibration frequency with f_w = 60 Hz on the top and f_w = 120 Hz on the bottom of the image; white arrows indicating the low velocity pockets.

core, the impingement region, and the radial wall-jet region. However, due to the induced excitation, the flow field is more chaotic. The incoming fully developed jet (at 6.1 m/s) impacts the surface which is also moving in the direction of jet impingement at a speed (2.3 m/s for 60 Hz and 4.7 m/s for 120 Hz) resulting in additional disturbance to the flow field. Low-velocity pockets are seen (indicated by white arrows in figure 7) with an increase in f_w creating a weak stagnation zone in the jet core. The corresponding pressure field is also altered. These changes to the flow field directly affect the thermal signatures on the impingement surface.

The resulting thermal changes on this moving impingement surface is now briefly discussed. The Nusselt number distribution for the vibrating impingement wall is shown in figure 8 for equispaced phases, ϕ = 0/8 to 7/8 of impingement wall oscillation cycle where phase, ϕ = 0/8 corresponds to y/D = 2.0 from which the surface moves upwards. The maximum heat transfer is observed within the region $r/D \leq 1$ when the impingement surface has reached its positive maximum. The location of local increase in heat-transfer moves radially outward with the upward movement of the impingement wall coinciding with the movement of the large eddies. The intensity of the Nu decreases with the reduction in the strength of these large eddies as they are convected downstream in the radial direction. The shedding frequency of the jet matches the applied frequency of wall vibration which corresponds to $St \approx 0.45$.

Conclusions

The present LES study validates a canonical jet-impingement configuration and further presents baseline cases for a jet impacting on a surface vibrating vertically at frequencies that are sub-harmonic and harmonic to the fundamental frequency of

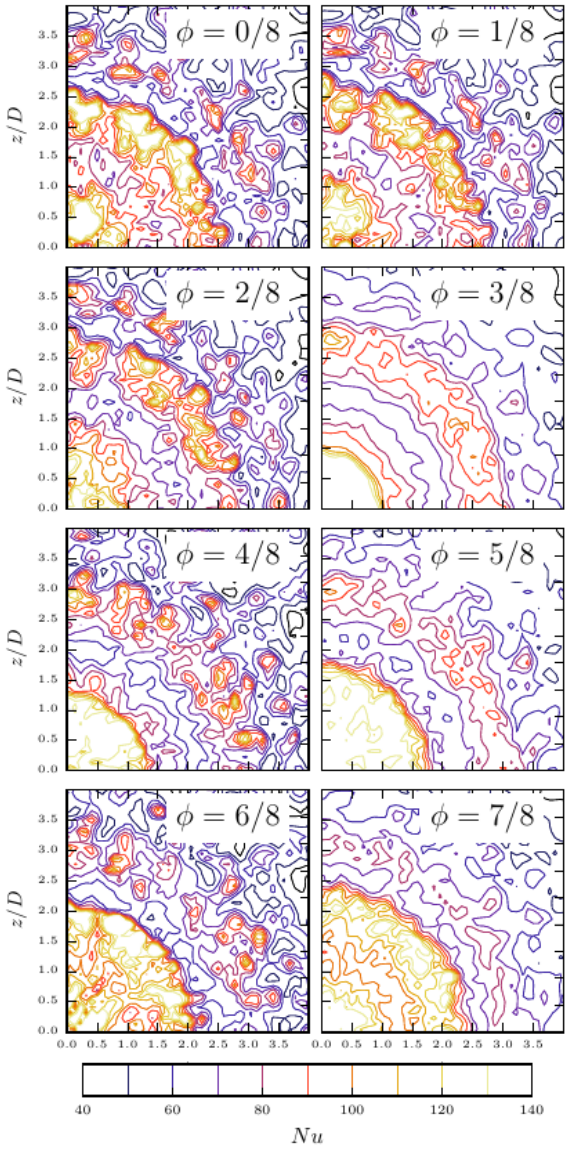

Figure 8: Contours of instantaneous Nusselt number for vibrating surface at f_w = 120 Hz

the jet. Induced vibration causes the complexity of the flow field to increase and significant variations to the flow field and heat transfer on the surface to occur. Increasing the frequency of vibration to the harmonic range increases the low velocity pockets or zones in the flow field, particularly in the stagnation region. This results in a highly unsteady flow field which can significantly affect the heat transfer. These results indicate that surface vibration can be used to alter the heat-transfer rates and their distribution on the jet-impingement surface and calls for further in-depth investigation to establish a clear correlation between the vibration frequencies and the resulting heat transfer.

Acknowledgements

Financial support from the Australian Research Council [ARC DP130103271] is gratefully acknowledged. This work was supported by resources provided by the Pawsey Supercomputing Centre with funding from the Australian Government and the Government of Western Australia.

References

[1] Baughn, J. W. and Shimizu, S., Heat transfer measurements from a surface with uniform heat flux and an impinging jet, *Journal of Heat Transfer*, **111**, 1989, 1096–1098.

[2] Cooper, D., Jackson, D., Launder, B. and Liao, G., Impinging jet studies for turbulence model assessment–I. Flow-field experiments, *International Journal of Heat and Mass Transfer*, **36**, 1993, 2675–2684.

[3] Dairay, T., Fortuné, V., Lamballais, E. and Brizzi, L.-E., Direct numerical simulation of a turbulent jet impinging on a heated wall, *Journal of Fluid Mechanics*, **764**, 2015, 362–394.

[4] Den Toonder, J. and Nieuwstadt, F., Reynolds number effects in a turbulent pipe flow for low to moderate Re, *Physics of Fluids (1994-present)*, **9**, 1997, 3398–3409.

[5] Eggels, J., Unger, F., Weiss, M., Westerweel, J., Adrian, R., Friedrich, R. and Nieuwstadt, F., Fully developed turbulent pipe flow: a comparison between direct numerical simulation and experiment, *Journal of Fluid Mechanics*, **268**, 1994, 175–210.

[6] Gardon, R. and Akfirat, J. C., The role of turbulence in determining the heat-transfer characteristics of impinging jets, *International Journal of Heat and Mass Transfer*, **8**, 1965, 1261–1272.

[7] Guala, M., Hommema, S. and Adrian, R., Large-scale and very-large-scale motions in turbulent pipe flow, *Journal of Fluid Mechanics*, **554**, 2006, 521–542.

[8] Lee, D., Greif, R., Lee, S. J. and Lee, J. H., Heat transfer from a flat plate to a fully developed axisymmetric impinging jet, *Journal of Heat Transfer*, **117**, 1995, 772–776.

[9] Lee, Jungho Lee, S.-J., Stagnation Region Heat Transfer of a Turbulent Axisymmetric Jet Impingement, *Experimental Heat Transfer*, **12**, 1999, 137–156.

[10] Lilly, D. K., A Proposed Modification of the Germano-Subgrid-Scale Closure Method, *Physics of Fluids A:Fluid Dynamics*, **4**, 1992, 633–635.

[11] Morrison, J., McKeon, B., Jiang, W. and Smits, A., Scaling of the streamwise velocity component in turbulent pipe flow, *Journal of Fluid Mechanics*, **508**, 2004, 99–131.

[12] Natarajan, T., Jewkes, J., Lucey, A., Narayanaswamy, R. and Chung, Y. M., Large-eddy simulations of a turbulent round jet impinging on a vibrating heated wall, *International Journal of Heat and Fluid Flow*, (under review).

[13] Viskanta, R., Heat transfer to impinging isothermal gas and flame jets, *Experimental Thermal and Fluid Science*, **6**, 1993, 111–134.

[14] Weller, H. G., Tabor, G., Jasak, H. and Fureby, C., A tensorial approach to computational continuum mechanics using object-oriented techniques, *Computers in physics*, **12**, 1998, 620–631.